Eddy-mean flow interactions and vertical eddy energy redistribution associated with the standing meander in the Antarctic Circumpolar Current

Takuro Matsuta[1] and Yukio Masumoto[1,2]

[1]Department of Earth and Planetary Science, Graduate School of Science, the University of Tokyo, Tokyo, Japan

[2]Application Laboratory, Japan Agency for Marine-Earth Science and Technology, Yokohama, Japan

Corresponding author: Takuro Matsuta (matsuta@eps.s.u-tokyo.ac.jp)

Key Points:

- The baroclinic energy conversion dissipates 55% of the local wind energy input within the standing meander region.
- The vertical eddy energy flux redistributes the eddy kinetic energy in vertical within the standing meander region.
- The eddy effects are negligible outside the standing meander region.

Abstract

Recent studies suggest that local eddy-mean flow interactions associated with standing meanders play key roles in the dynamics of the Antarctic Circumpolar Current. Here we explore the importance of the local dynamics quantitatively with a viewpoint of energy transfer using the Lorentz diagram concept. Results confirm the importance of the eddy-mean flow interactions in the standing meander, showing that 55% of the wind energy input is converted to the eddy energy through the baroclinic instability in the standing meander region. It is also found that most of the eddy kinetic energy is dissipated local in the deeper layer due to the vertical energy redistribution governed by the vertical pressure flux. Contrary, the eddy effects are negligible outside the standing meander region.

Plain Language Summary

The insensitivity of the Antarctic Circumpolar Current transport to changes in wind stress is thought to be caused by a secondary circulation due to mesoscale eddies. Previous studies have pointed out qualitatively that the eddy-mean flow interactions occur rather limited region near standing meanders, but its quantitative evaluation of associated processes has not been conducted. This study thus explores the importance of the local dynamics quantitatively using the Lorentz diagram concept. Our results indicate that the baroclinic instability efficiently transfer the wind energy input to the eddy energy within the standing meander regions. Only five major standing meanders can provide most of the baroclinic energy transfer for the entire Southern Ocean. It is also shown that the vertical pressure flux is responsible for the vertical energy transport from the eddy energy generation sites in the upper 3000 m depth down to the deeper layer, where the eddy energy dissipation mainly occurs.

1 Introduction

It has been suggested that total time-mean volume transport of the Antarctic Circumpolar Current (ACC) and associated local meridional overturning circulation is insensitive to changes in wind forcing (e.g. Hogg et al. 2008; Munday et al. 2013; Thompson and Naveira Garabato 2014; Constantinou and Hogg 2019). This phenomenon often referred to as "eddy saturation" is explained through a balance between the wind-driven Ekman transport and the eddy-induced counter transport in the zonally averaged framework (e.g. Marshall and Radko 2003; Marshall and Speer 2012; Munday et al. 2013; Youngs et al. 2019). This zonally averaged view, however, conceals the ACC's complex frontal structures and eddy characteristics in the zonal direction (Thompson and Naveira Garabato 2014 and references therein, hereafter TG2014). For example, TG2014 suggested that large eddy activities are localized in the vicinity of standing meanders associated with the significant topography and that eddy-mean flow interactions are quite weak in the regions far from the standing meanders. Their analysis based on the Eliassen-Palm tensor (Plumb, 1986) revealed that the eddy forcing along the streamlines decelerates the mean flow within the meandering sections in the equilibrium state. TG2014 also showed that the increased transport driven by the wind forcing enhances the meander curvature, resulted in enhanced eddy kinetic energy (EKE). The large eddy activities strengthen the vertical momentum transport due to baroclinic instability, which in turn changes the baroclinic structure of the meander and decreases the mean flow. They indicated qualitative importance of this localized negative feedback mechanism in the eddy saturation and suggested necessity of a quantitative evaluation of the process.

Here we explore the importance of the local dynamics quantitatively with the viewpoint of the Lorentz diagram concept (Lorentz, 1955). Although the eddy-mean flow energy transfer

over the entire Southern Ocean has already been analyzed in several previous literatures with realistic models (Chen et al., 2014; Wu et al., 2017; Jüling et al., 2018), suggesting that baroclinic instability dominates the generation of EKE, its spatial structure has not been investigated. On the other hand, Youngs et al. (2017) has shown that the mixed barotropic and baroclinic instability is important in the region of standing meanders using an idealized model, but not for a realistic condition. In this study, detailed energy transfer, including the vertical component of energy flux, is investigated using the local Lorentz diagram applied to the standing meander region appeared in a realistic eddy-resolving model. Our results support the importance of the local negative feedback hypothesis suggested by TG2014 and, in addition, give a clearer insight into vertical energy redistribution associated with the eddy-mean flow interactions, which is missing from the canonical Lorentz diagram analysis.

2 Model Data

Results from an eddy-resolving Ocean General Circulation Model (OGCM), named OGCM for the Earth Simulator (OFES) (Masumoto et al., 2004), are used in the following analyses. OFES is based on the Modular Ocean Model ver. 3 (MOM3) developed at GFDL (Pacanowski & Griffies, 2000) and optimized for the massively-parallel computational architecture of the Earth Simulator. The horizontal grid spacing is 0.1° x 0.1° and there are 54 vertical levels. The 3-day snapshots for a period of 2001-2010, driven by the NCEP reanalysis products as the surface boundary forcing, are used (see Sasaki et al. (2006, 2008) for more detailed model settings). It has been shown that OFES captures variability in the Southern Ocean realistically (e.g. Masumoto, 2010; TG2014), providing a reasonable platform to examine the

83 eddy-mean flow interactions in the ACC. It is confirmed that following results are qualitatively
84 the same for different analysis periods.

85

86 **3 Method**

87 We consider a variable x that can be described by its temporal average $\overline{x}$ and eddy
88 perturbations x' as a deviation from the temporal average, i.e.,

89 $$x' = x - \overline{x}. \tag{1}$$

90 With this separation between the mean field and eddy turbulences, the mean kinetic and
91 available potential energy are respectively defined as

92 $$K_M = \frac{1}{2}\rho_0\left(\overline{u}^2 + \overline{v}^2\right), \tag{2}$$

93 $$P_M = -\frac{1}{2}\frac{g}{n_0}\,\overline{\rho^*}^2, \tag{3}$$

94 and the eddy kinetic energy (EKE) and the eddy available potential energy are defined as

95 $$K_E = \frac{1}{2}\rho_0\left(\overline{u'^2} + \overline{v'^2}\right), \tag{4}$$

96 $$P_E = -\frac{1}{2}\frac{g}{n_0}\,\overline{\rho'^2}\,. \tag{5}$$

97 Here, n_0 is the globally averaged, time mean vertical gradient of the potential density referenced
98 to a depth of 2000 m (Von Storch et al., 2012). The variation of the density is defined by

99 $$\rho^* = \rho - \langle\overline{\rho}\rangle\,, \tag{6}$$

100 where $\langle\overline{X}\rangle$ means the temporal and global average of the value X.

According to Chen et al., (2014), the mean flow and eddy energy equations satisfy

$$\frac{\partial}{\partial t}K_M + \nabla(\overline{\boldsymbol{u}}K_M) + \rho_0\nabla\left(\overline{u}\overline{u'\boldsymbol{u'}} + \overline{v}\overline{v'\boldsymbol{u'}}\right) + \nabla\left(\overline{\boldsymbol{u}}\overline{p^*}\right) = -g\overline{\rho^*}\overline{w} - \rho_0\left[-\overline{u'\boldsymbol{u'}}\cdot\nabla\overline{u} - \overline{v'\boldsymbol{u'}}\cdot\nabla\overline{v}\right] + S(K_M), \tag{7}$$

$$\frac{\partial}{\partial t}K_E + \nabla\left(\overline{\boldsymbol{u}}K_E + \overline{\boldsymbol{u'}\frac{1}{2}\rho_0\left(u'^2 + v'^2\right)}\right) + \nabla\left(\overline{\boldsymbol{u'}p'}\right) = -g\overline{\rho'w'} + \rho_0\left[-\overline{u'\boldsymbol{u'}}\cdot\nabla\overline{u} - \overline{v'\boldsymbol{u'}}\cdot\nabla\overline{v}\right] + S(K_E) \tag{8}$$

$$\frac{\partial}{\partial t}P_M + \nabla(\overline{\boldsymbol{u}}P_M) + \nabla_h\cdot\left(-\overline{\rho'\boldsymbol{u}_h'}\,\frac{g}{n_0}\overline{\rho^*}\right) = g\overline{\rho^*}\overline{w} - \frac{g}{n_0}\overline{\rho'\boldsymbol{u}_h'}\cdot\nabla_h\overline{\rho} + S(P_M), \tag{9}$$

$$\frac{\partial}{\partial t}P_E + \nabla(\overline{\boldsymbol{u}}P_E) + \nabla\cdot\left(-\frac{g}{2n_0}\overline{\boldsymbol{u'}\rho'^2}\right) = g\overline{\rho'w'} + \frac{g}{n_0}\overline{\rho'\boldsymbol{u}_h'}\cdot\nabla_h\overline{\rho} + S(P_E), \tag{10}$$

where $\boldsymbol{u}$ is the three-dimensional velocity vector, $\boldsymbol{u_h}$ is the horizontal component of the velocity, ∇ is the three-dimensional gradient operator, ∇_h is the horizontal gradient operator, p is the combined sea surface elevation and hydrostatic pressure, $p^* = p - \langle\overline{p}\rangle$, $S(\cdot)$ is the source/sink term calculated as the residual from the respective balance equation. The second term of the right-hand side in the equations (7) and (8), i.e.

$$BTR = \rho_0\left[-\overline{u'\boldsymbol{u'}}\cdot\nabla\overline{u} - \overline{v'\boldsymbol{u'}}\cdot\nabla\overline{v}\right], \tag{11}$$

is the barotropic conversion rate (BTR) due to eddy-mean flow interactions. Positive values of BTR means that the barotropic instability transfers the mean flow energy into the EKE. Similarly, the second term of the right-hand side of the equations (9) and (10), i.e.

$$BCR = \frac{g}{n_0}\overline{\rho'\boldsymbol{u}_h'}\cdot\nabla_h\overline{\rho}, \tag{12}$$

116 is the baroclinic conversion rate (BCR), whose positive sign indicates that eddies extract the
117 mean available potential energy from the mean stratification. The first term of the right-hand side
118 of the equation (8) and (10), i.e.

119 $$VEDF = -g\overline{\rho' w'}\,,$$

120 is the vertical eddy density flux (VEDF), which releases the eddy available potential energy
121 generated due to baroclinic instability. Positive values of the VEDF are associated with the
122 convective process, with dense fluid sinking and light fluid rising (Zhai & Marshall, 2013; Aiki
123 et al., 2016). The third term of the left-hand side of (8), i.e. $\nabla\left(\overline{\boldsymbol{u}' p'}\right)$, is the energy flux by the
124 eddy pressure work, of which the vertical component $\partial_z\left(\overline{w' p'}\right)$ represents redistribution of the
125 EKE in vertical (Zhai & Marshall, 2013).

126 Noted here that the available potential energies in the form of (3) and (5) are not the
127 exact conservative quantities (Von Storch et al., 2012; Chen et al., 2014; Aiki et al., 2016), and
128 resultant conservation equations of (9) and (10) are the approximate forms (Chen et al., 2014;
129 Aiki et al., 2016; Wu et al., 2017). Aiki et al. (2016) proposed the exact form of the eddy
130 available potential energy, independent of the choice of the background density profile, without
131 any assumptions and derived the associated conservation law. However, their eddy available
132 potential energy is not well-defined in the mixed-layer and inside the weakly stratified water
133 mass such as the Subantarctic Mode Water (McCartney, 1979). Therefore, we use the
134 approximated energy equations of (7) - (10) in the present study. It should be noted here,
135 however, that our results do not change qualitatively when we use the exact Lorentz diagram of
136 Aiki et al. (2016).

4 Results

4.1 Basic structures of the standing meander

We focus on the standing meander of the ACC in the region 45˚S - 60˚S, 25˚E - 40˚E in this study. This choice is arbitrary, but resultant energy pathways in other standing meanders are almost the same (see the supplement materials). Horizontal distributions of the EKE in the upper layer at a depth of 207 m and the sea surface elevation averaged from 2001 to 2010 simulated in OFES are shown in Figure 1a. The strong eastward flow associated with the ACC is mainly located within a region bounded by the sea surface elevation contours of -0.4 m and -1.6 m. The contours of the sea surface elevation are closely packed in the upstream region (west of 35˚E), while downstream of the meander (east of 35˚E) the ACC jet broadens. Inside the meander, the EKE values exceed $1000\ \mathrm{cm^2\ s^{-2}}$. Regions of relatively large EKE values are also observed along the 3000 m isobath between 40˚E and 50˚E in spite of the weak sea surface elevation gradient. On the other hand, the EKE is very weak far from the standing meander region, indicating non-uniformity of the ACC in the zonal direction. The horizontal distribution of the EKE in the deeper layer at a depth of 2119 m (Figure 1b) has a coherent structure with that of the surface EKE. The EKE values are larger than $80\ \mathrm{cm^2\ s^{-2}}$ within the longitude band of the standing meander, while they are smaller than $20\ \mathrm{cm^2\ s^{-2}}$ outside the standing meander. All these features of the EKE are consistent with the previous studies (e.g. TG2014 and references therein).

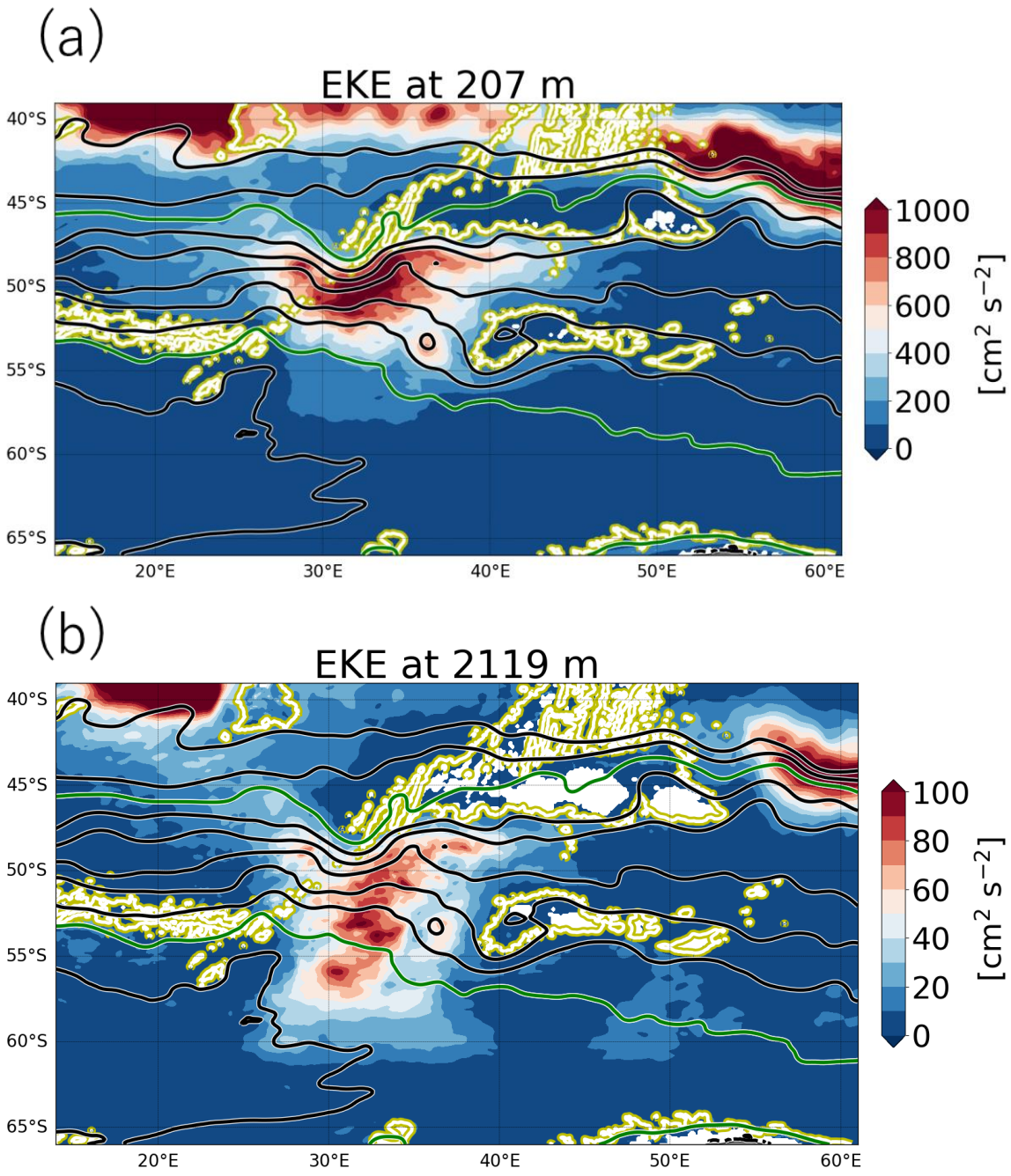

Figure 1. Horizontal distributions of the EKE at a depth of (a) 207 m and (b) 2119 m. Black and green contours in (a) represent the sea surface elevation with a contour interval of 0.2 m, with green lines indicate the -0.4 m and -1.6 m contours as the boundaries of the ACC. The yellow-edged white contours indicate the 3000 m isobath.

4.2 Horizontal distribution of the energy conversion rate

Figure 2 shows spatial distributions of the mean wind energy input, the BTR, and the VEDF. The mean wind energy input is calculated using $W_{wind} = \overline{\boldsymbol{\tau}} \cdot \overline{\boldsymbol{u_0}}$, where $\overline{\boldsymbol{\tau}}$ is the mean surface wind stress and $\overline{\boldsymbol{u_0}}$ is the mean total surface velocity (Zhai & Marshall, 2013) . Since the BCR includes the rotational component which doesn't contribute to the eddy-mean flow energy transfer (Marshall & Shutts, 1981), it would be useful to examine the VEDF as the baroclinic energy pathway instead (Chen, 2013). According to Figure 2a, the surface wind forcing is uniformly distributed along the ACC path. The westerlies are as high as 0.2 N m^{-2} between the sea surface elevation contours of -0.4 m and -1.6 m. Reflecting the homogeneous distribution of wind stress, the energy input is also large in a wide area within the ACC, exceeding 4.0×10^{-2} W m^{-2}. The atmospheric winds thus tend to homogeneously accelerate the ACC.

On the other hand, large values of the BTR and VEDF are highly confined in the standing meander region, bounded by the 25˚E and 40˚E longitude lines zonally and by -0.4 m and -1.6 m sea surface elevation contours meridionally (SM region hereafter) (Figure 2b,c). The elongated dipole structures of the BTR are observed in the region 47˚S - 50˚S, 33˚E -38˚E, where the contours of sea surface elevation are densely packed together. The area-integrated BTR in the SM region is 0.2 GW , which is only 0.5% of the wind energy input, indicating that the barotropic instability plays a minor role in the dynamics in the standing meander. Unlike the BTR, the VEDF (Figure 2c) is uniformly large inside the SM region, suggesting that eddies systematically work to flatten isopycnals. As is expected from the linear theory of the baroclinic instability (e.g. Olbers et al. 2012), the EKE generation through the VEDF follows the location

of the mean sea surface elevation gradients. Values of the VEDF exceeds 8.0×10^{-2} W m^{-3} at around the center of the standing meander and larger than 4.0×10^{-2} W m^{-3} at the flank of the jet. The area-integrated value of the VEDF in the SM region reaches 21 GW, which is nearly 55% of the local mean wind energy input. This result is consistent with previous works using realistic eddy-resolving models (Zhai & Marshall, 2013; Aiki et al., 2016), which has shown that the wind energy input to the gyre circulation is largely balanced by the VEDF. It is also worth noting that this VEDF distribution differs slightly from that of the EKE distribution (Figure 1). The eddy production is larger between 25˚E and 35˚E compared to that in the region east of 35˚E even within the SM region, whereas relatively large values of the EKE extend to the east of 35˚E. The area-integrated EKE advection i.e. $\nabla(\overline{\boldsymbol{u}}\overline{K_E})$ in the eastern part of SM region between 35˚E and 40˚E is 3.0 GW, which is comparable to the VEDF value of 3.8 GW within the same region, suggesting that transient eddies are advected downstream from a region of the initial baroclinic growth as pointed out in previous researches (Abernathey & Cessi, 2014; Bischoff & Thompson, 2014; Thompson & Garabato, 2014; Chapman et al., 2015; Youngs et al., 2017).

In the downstream region, bounded by the 40˚E and 55˚E longitude lines zonally and -0.4 m and -1.6 m sea surface elevation contours meridionally (DS region hereafter) (see Fig.2b for the location), the baroclinic conversion is weak in spite of the strong energy input by the wind forcing. While the wind energy input is 44 GW in the DS region, the value of VEDF is only 1.6 GW. The barotropic conversion also has little contributions to the EKE balances. These features demonstrate that the energy cascade by eddy-mean flow interactions is localized within the SM region, which is consistent with the result of TG2014.

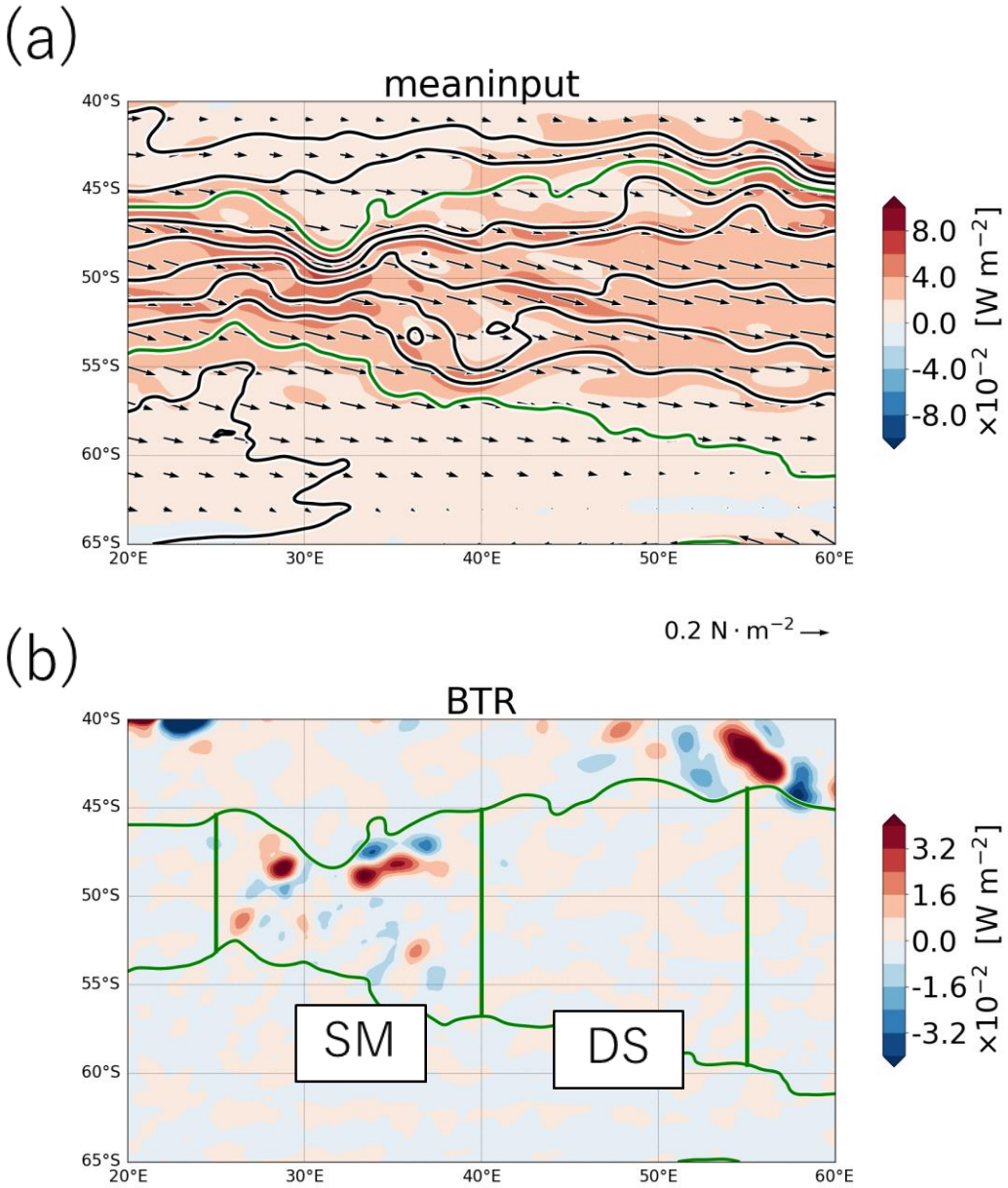
(a)
meaninput
40°S
45°S
50°S
55°S
60°S
65°S
20°E
30°E
40°E
50°E
60°E
8.0
4.0
0.0
-4.0
-8.0
×10⁻² [W m⁻²]
(b)
0.2 N · m⁻²
BTR
SM
DS
3.2
1.6
0.0
-1.6
-3.2
×10⁻² [W m⁻²]

206

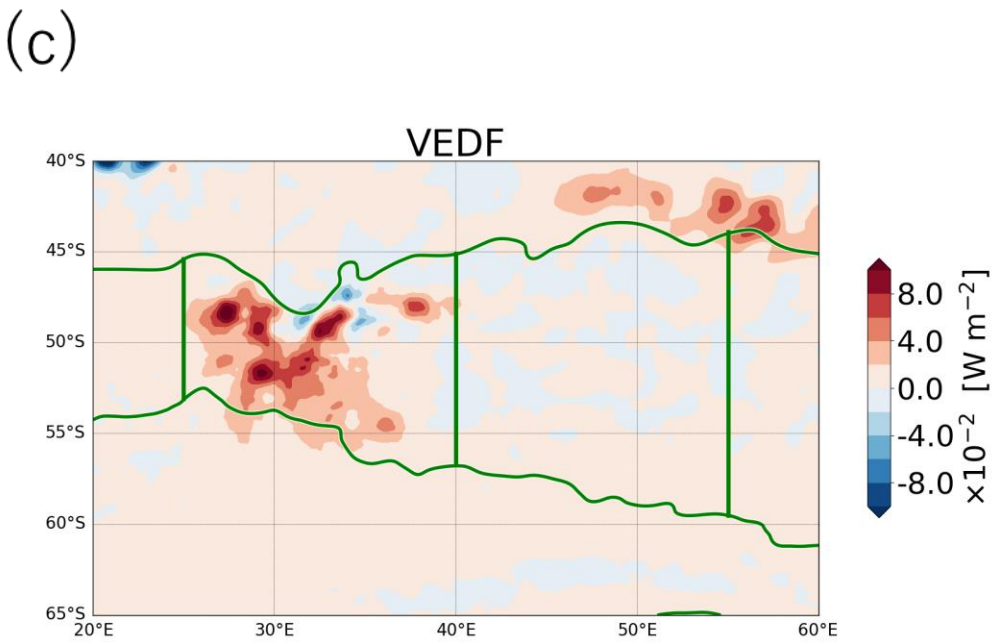

Figure 2. Horizontal distributions of (a) the mean wind energy input, (b) the BTR, and (c) the VEDF. The black arrows in (a) represent the mean wind stress. The black and green contours in (a) are the same as those in Figure 1. The region bounded by two green contours representing the northern and southern boundaries of the ACC is further divided into the standing meander (SM) region and the downstream (DS) region by 25˚E, 40˚E, and 55˚E longitude lines and shown in (b) and (c).

The Lorentz diagram shown in Figure 3 summarizes more detailed energy pathways, including the energy transfer discussed above, focusing on the eddy energy budget. It is noted that non-local eddy-mean flow interactions (Murakami, 2011; Chen et al., 2014, 2016) is confirmed to be negligible in our target region, therefore we don't treat the non-local interactions in this paper. The baroclinic conversion rate BCR in the SM region is as large as $22\ \mathrm{GW}$, which is nearly equal to that of the VEDF. This large values of the BCR suggest that the eddy induced density transport effectively runs across the mean density contours and weakens the isopycnal slope. Almost all the extracted energy by the baroclinic instability is released from the stratification through the VEDF as seen in the above discussion. Since the barotropic energy conversion rate and advective fluxes are weak in the SM region, almost all the converted EKE through the baroclinic instability is dispersed locally by the viscosity and the bottom drag. On the other hand, the energy sink in the form of the eddy available potential energy is only $1.6\ \mathrm{GW}$. Therefore, more than a half of the local energy input by the winds is dissipated through the baroclinic energy pathway $P_M \rightarrow P_E \rightarrow K_E$ in the SM region, which is similar to the energy pathway obtained for the entire ACC region (Chen et al. 2014; Wu et al. 2017; Jüling et al. 2018 and Supplement in this paper).

In the DS region, on the other hand, the baroclinic conversion rate is very small, while the wind input is comparable to that in the SM region. Only 5% of the energy gain is cascaded to the eddy fields, indicating that the energy sink by the eddy-mean flow interactions is localized in the SM region. This result suggests that a limited area of the ACC showing the standing meander is possibly responsible for the baroclinic energy pathway of the entire Southern Ocean as hypothesized by TG2014. In fact, the VEDF (the EKE dispersion) integrated in the five major

238 standing meander regions along the ACC reaches 74% (67%) of the VEDF (the EKE dispersion)
239 integrated over the entire ACC (see Supplement).
240

241

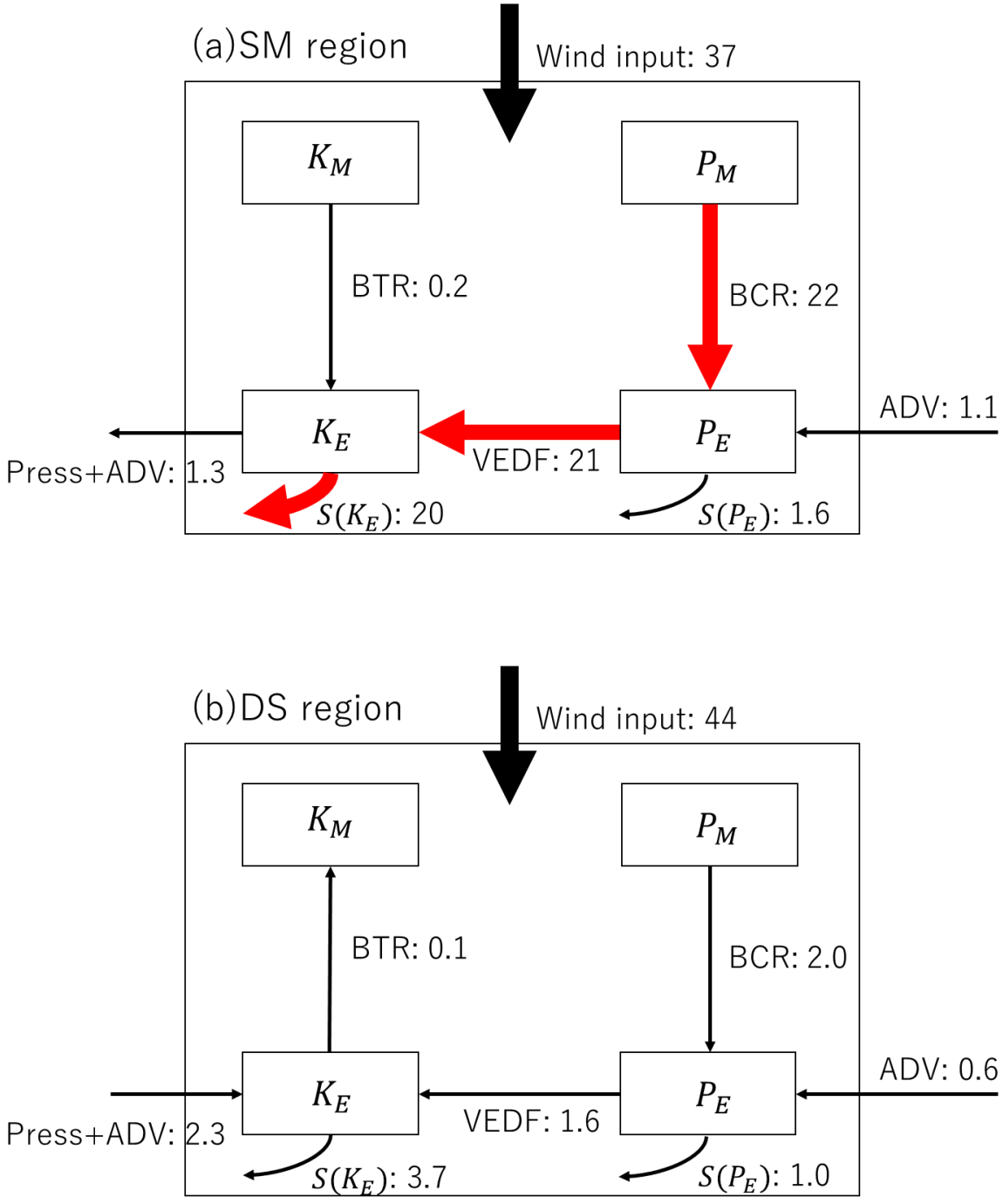

242

243 Figure 3. The Lorentz energy diagram in GW (10^9W) calculated in the SM region (upper

244 diagram) and the DS region (lower diagram), respectively. Black and red arrows connecting the

four boxes represent the energy transfer associated with the barotropic conversion (BTR), the baroclinic conversion (BCR), and the vertical eddy density flux (VEDF). The curved arrow of $S(K_E)$ ($S(P_E)$) connected to the K_E (P_E) box indicates the energy source/sink in the equation (8) (the equation (10)).

250

251 4.3 The vertical energy transfer

252 Figure 4 shows vertical distributions of the VEDF, source/sink of the EKE i.e. $S(K_E)$ of
253 (8), divergence of the eddy pressure flux $\nabla(\overline{\boldsymbol{u}'p'})$, and its difference from the vertical component
254 $\partial_z(\overline{w'p'})$. Each value is obtained by averaging over the meridional extent of the envelope
255 bounded by the -0.4 m and -1.6 m sea surface elevation contours. This choice of the
256 boundaries is arbitrary, but following results do not change with a different choice of bounded
257 contours.

258 According to Figure 4a, the EKE generation has a deep structure with its maximum
259 strength in the upper 1000 m depth and relatively strong values penetrate down to a depth deeper
260 than 3000 m. This feature is different from the vertical structure of VEDF in both the subtropical
261 gyre, where the large VEDF is surface-intensified, and the subpolar gyre, where the maximum of
262 VEDF appears around a depth of 2000 m, in the North Atlantic (Zhai & Marshall, 2013). The
263 zonal position of the active eddy generation area follows the location of the standing meander.
264 Although the VEDF is relatively small in the eastern part of the SM region (35˚E - 40˚E), it has
265 also a deep structure reaching a depth of 3000 m.

266 The distribution of the source/sink terms (Figure 4b) is different from that of the VEDF.
267 Strong EKE dissipation, i.e. the energy sink, are observed within the upper 500 m depth or the
268 layer below 3000 m depth in the SM region. This mismatch in the vertical location between the
269 energy generation and the energy sink can be reconciled through the non-local process by the
270 pressure flux (Figure 4c). While the energy flux by the pressure work converges in the lower
271 layer deeper than 3000 m depth, it diverges in the upper 3000 m depth, where the EKE

production is prominent as seen in Figure 4a. This vertical communication seems to be achieved by the vertical pressure flux $\overline{w'p'}$, which shows downward flux throughout the water column east of 30˚E. The eddy energy flux thus acts to make the flow more barotropic inside the standing meander. In the region west of 30˚E, the vertical pressure flux is upward near the surface and downward in the deeper layer with the separation boundary at around 2000 m depth. This upward flux in the upper layer of the upstream region may be related to the increase in the baroclinicity of the flow by the along-stream eddy forcing shown in TG2014. To confirm that the vertical communication is dominated by the vertical energy flux, we calculate the difference between $\nabla(\overline{\boldsymbol{u}'p'})$ and $\partial_z(\overline{w'p'})$ (Figure 4d). The difference is quite small in the layer below 1000 m depth, although there are signatures of small-scale noises in the depth below 4000 m depth. Therefore, it is concluded that the EKE is generated in the upper 3000 m depth and the eddy energy is transported downward by the vertical pressure flux. The eddy energy converged near the bottom may be dissipated by the bottom friction and the viscosity in OFES. In reality, energy dissipation associated with small-scale processes, such as the generation of internal waves by the topography, may be important as the energy sink.

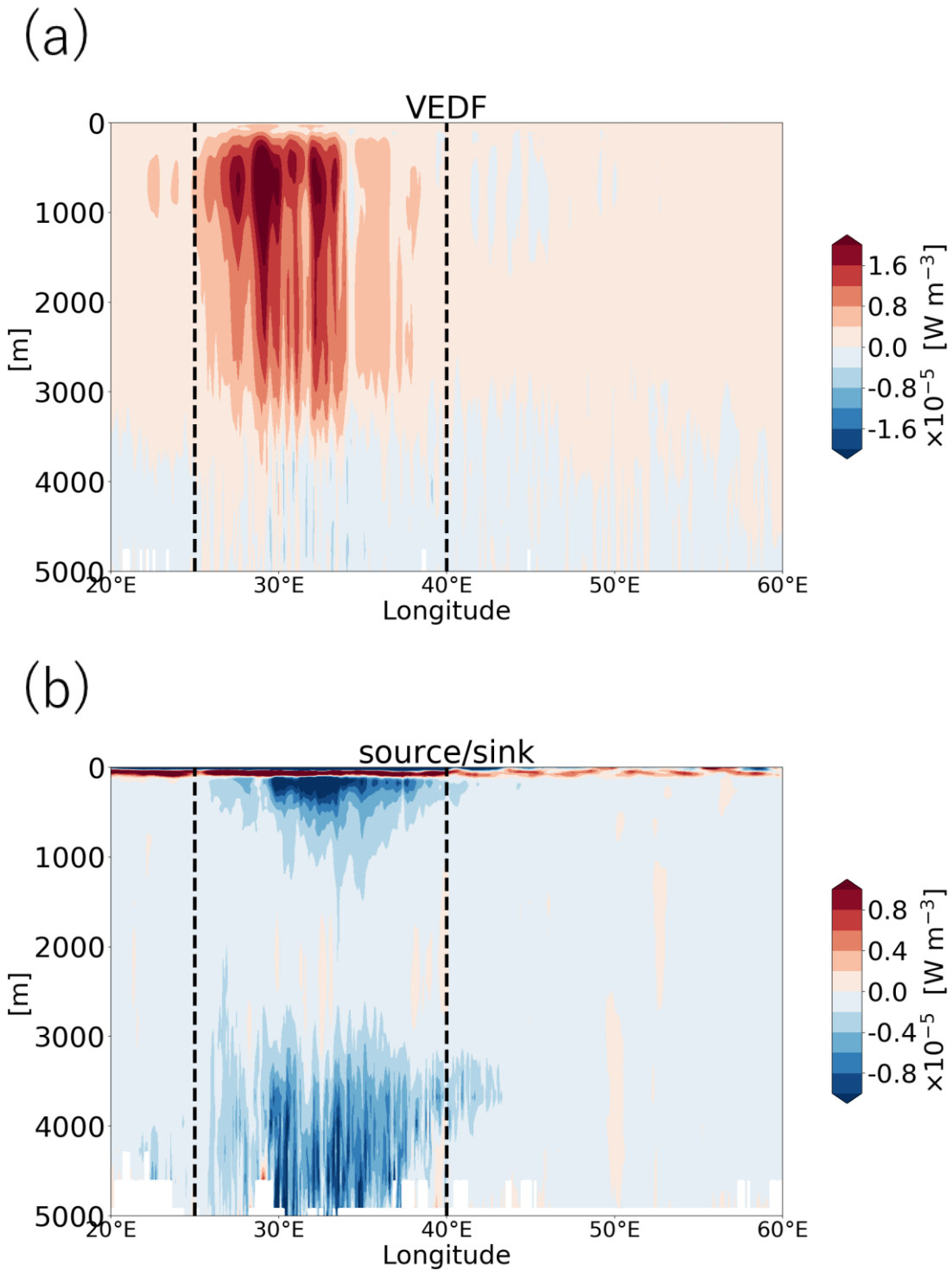
(a)
VEDF
0
1000
2000
3000
4000
5000
[m]
20°E
30°E
40°E
50°E
60°E
Longitude
1.6
0.8
0.0
-0.8
-1.6
×10⁻⁵ [W m⁻³]
(b)
source/sink
0
1000
2000
3000
4000
5000
[m]
20°E
30°E
40°E
50°E
60°E
Longitude
0.8
0.4
0.0
-0.4
-0.8
×10⁻⁵ [W m⁻³]

289

290

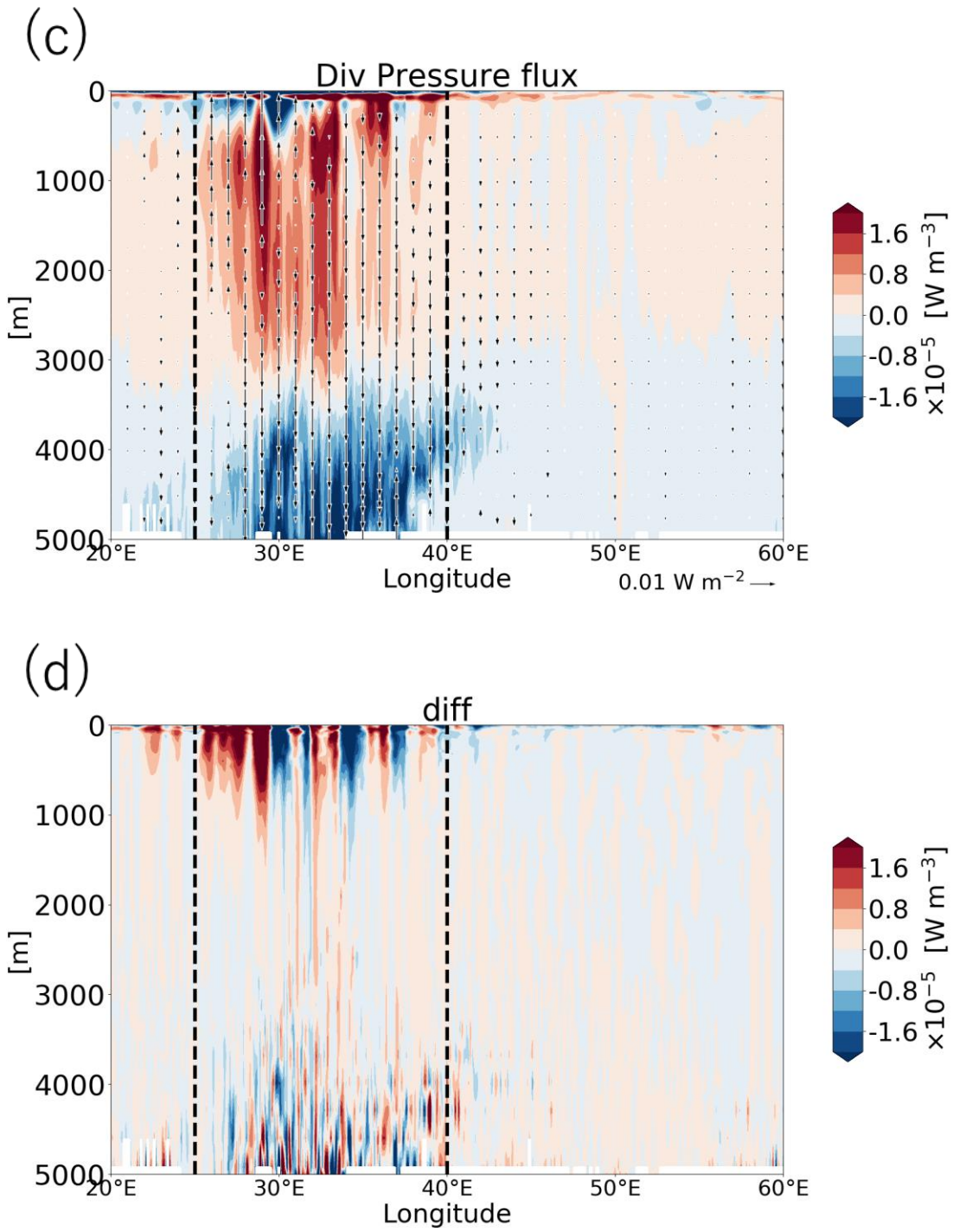

291

292 Figure 4. The vertical distribution of (a) the VEDF, (b) the eddy energy sources/sinks, (c) the

293 divergence of the pressure flux $\nabla(\overline{\boldsymbol{u}'p'})$, and (d) the differences between the divergence of the

294 pressure flux and its vertical component $\partial_z(\overline{w'p'})$ averaged meridionally in the envelope defined
295 by -0.4m and -1.6m seas surface elevation contours. The black arrows in (c) represent the
296 vertical energy flux $\overline{w'p'}$ in W m^{-2}. The vertical black dotted lines at 25˚E and 40˚E indicate the
297 western and eastern boundary of the standing meander region, respectively.
298

5 Discussion and Conclusions

We have evaluated the energy pathways and the role of vertical energy flux in the standing meander region of the ACC using outputs of an eddy resolving OGCM from the viewpoint of the eddy-mean flow interactions. The analysis of the Lorentz diagram reveals that more than a half of the wind energy input is converted to the eddy energy through the baroclinic conversion $P_M \rightarrow P_E \rightarrow K_E$ in the standing meander region. In the downstream region, the wind energy input has the same magnitude as that in the standing meander region, whereas the eddy-mean flow interactions no longer work efficiently. The eddy kinetic energy generation occurs mainly in the layer shallower than 3000 m depth. It is the vertical pressure flux that transport the EKE from the generation sites to the deeper layer, where the energy dissipation mainly occurs. The pressure flux, therefore, plays a key role for the vertical energy redistribution although it is shown to have only a minor role in the integrated viewpoint of the Lorentz diagram (see Supplement for the schematic map of our findings).

These results suggest that the eddy-mean flow interactions in the standing meander region play a significant role in relaxing changes in the wind forcing. In fact, the dissipation of EKE integrated only in the five major meanders reaches 22% of the total mean wind energy input and 67% of the EKE dissipation over the entire ACC region (see Supplement), supporting importance of the local negative-feedback mechanism of the eddy saturation suggested in TG2014.

The energy dissipation except for the standing meander regions is a remaining problem. Although the baroclinic conversion rate can balance the local wind forcing, it is insufficient to

dissipate all the energy gained over the entire ACC. Recently, Youngs et al. (2019) suggested using the two-layer quasigeostrophic channel model that the residual overturning circulation is also important for the eddy saturation as well as the processes associated with a topography. Armour et al. (2016) showed that the surface heat advection may also contribute to the energy export from the Southern Ocean, although their model is too coarse to resolve eddy effects. Since the energy pathways in the idealized model could be different from that in the realistic model, these mechanisms should be tested using outputs of realistic eddy-resolving models. The estimation of the three-dimensional residual circulation in a realistic OGCM is challenging and needs further investigation.

Acknowledgments

This work was supported by a JSPS Grant-in-Aid for Scientific Research(A) (17H01663) and a JSPS Grant-in-Aid for Transformative Research Areas(B) (20H05731). OFES data and its information are available in http://www.jamstec.go.jp/datadoi/doi/10.17596/0002029.html.

References

Abernathey, R., & Cessi, P. (2014). Topographic enhancement of Eddy efficiency in baroclinic equilibration. *Journal of Physical Oceanography*, *44*(8), 2107–2126. https://doi.org/10.1175/JPO-D-14-0014.1

Aiki, H., Zhai, X., & Greatbatch, R. J. (2016). Energetics of the global ocean: The role of mesoscale eddies. *World Scientific Series on Asia-Pacific Weather and Climate*, *7*, 109–134. https://doi.org/10.1142/9789814696623_0004

Armour, K. C., Marshall, J., Scott, J. R., Donohoe, A., & Newsom, E. R. (2016). Southern Ocean warming delayed by circumpolar upwelling and equatorward transport. *Nature Geoscience*, *9*(7), 549–554. https://doi.org/10.1038/ngeo2731

Bischoff, T., & Thompson, A. F. (2014). Configuration of a Southern Ocean storm track. *Journal of Physical Oceanography*, *44*(12), 3072–3078. https://doi.org/10.1175/JPO-D-14-0062.1

Chapman, C. C., Hogg, A. M. C., Kiss, A. E., & Rintoul, S. R. (2015). The dynamics of Southern Ocean storm tracks. *Journal of Physical Oceanography*, *45*(3), 884–903. https://doi.org/10.1175/JPO-D-14-0075.1

Chen, R. (2013). Energy pathways and structures of oceanic eddies from the ECCO2 state estimate and simplified models. *Energy Pathways and Structures of Oceanic Eddies from the ECCO2 State Estimate and Simplified Models*. https://doi.org/10.1575/1912/5793

Chen, R., Flierl, G. R., & Wunsch, C. (2014). A description of local and nonlocal eddy-mean flow interaction in a global eddy-permitting state estimate. *Journal of Physical Oceanography*, *44*(9), 2336–2352. https://doi.org/10.1175/JPO-D-14-0009.1

Chen, R., Thompson, A. F., & Flierl, G. R. (2016). Time-dependent eddy-mean energy diagrams and their application to the ocean. *Journal of Physical Oceanography*, *46*(9), 2827–2850. https://doi.org/10.1175/JPO-D-16-0012.1

Constantinou, N. C., & Hogg, A. M. C. (2019). Eddy Saturation of the Southern Ocean: A Baroclinic Versus Barotropic Perspective. *Geophysical Research Letters*, *46*(21), 12202–12212. https://doi.org/10.1029/2019GL084117

Firing, Y. L., Chereskin, T. K., & Mazloff, M. R. (2011). Vertical structure and transport of the Antarctic Circumpolar Current in Drake Passage from direct velocity observations. *Journal of Geophysical Research: Oceans*, *116*(8), 1–16. https://doi.org/10.1029/2011JC006999

Hogg, A. M. C., Meredith, M. P., Blundel, J. R., & Wilson, C. (2008). Eddy heat flux in the Sourthern ocean: Response to variable wind forcing. *Journal of Climate*, *21*(4), 608–620. https://doi.org/10.1175/2007JCLI1925.1

Jüling, A., Viebahn, J. P., Drijfhout, S. S., & Dijkstra, H. A. (2018). Energetics of the Southern Ocean Mode. *Journal of Geophysical Research: Oceans*, *123*(12), 9283–9304. https://doi.org/10.1029/2018JC014191

373 Killworth, P. D. (1992). An Equivalent-Barotropic Mode in the Fine Resolution Antarctic
374 Model. *Journal of Physical Oceanography*, *22*(11), 1379–1387.
375 https://doi.org/10.1175/1520-0485(1992)022<1379:AEBMIT>2.0.CO;2

376 Killworth, P. D., & Hughes, C. W. (2002). The antarctic circumpolar current as a free
377 equivalent-barotropic jet. *Journal of Marine Research*, *60*(1), 19–45.
378 https://doi.org/10.1357/002224002762341230

379 Lorentz, E. N. (1955). Available Potential Energy and the Maintenance of the General
380 Circulation. *Tellus*, *7*(2), 157–167. https://doi.org/10.1111/j.2153-3490.1955.tb01148.x

381 Marshall, J., & Radko, T. (2003). Residual-Mean Solutions for the Antarctic Circumpolar
382 Current and Its Associated Overturning Circulation. *Journal of Physical Oceanography*,
383 *33*(11), 2341–2354. https://doi.org/10.1175/1520-0485(2003)033<2341:RSFTAC>2.0.CO;2

384 Marshall, J., & Shutts, G. (1981). A Note on Rotational and Divergent Eddy Fluxes. *Journal of*
385 *Physical Oceanography*, *11*(12), 1677–1680. https://doi.org/10.1175/1520-
386 0485(1981)011<1677:ANORAD>2.0.CO;2

387 Marshall, J., & Speer, K. (2012). Closure of the meridional overturning circulation through
388 Southern Ocean upwelling. *Nature Geoscience*, *5*(3), 171–180.
389 https://doi.org/10.1038/ngeo1391

390 Masumoto, Y., Sasaki, H., Kagimoto, T., Komori, N., Ishida, A., Sasai, Y., et al. (2004). A fifty-
391 year eddy-resolving simulation of the world ocean: Preliminary outcomes of OFES (OGCM
392 for the Earth Simulator). *Journal of the Earth Simulator*, *1*(January), 35–56. Retrieved from
393 http://www.jamstec.go.jp/esc/publication/journal/jes_vol.1/pdf/JES1-3.2-masumoto.pdf

McCartney, M. S. (1979). Subantarctic Mode Water. *Woods Hole Oceanographic Institution Contribution*, *3773*, 103–119. Retrieved from http://oceanrep.geomar.de/48397/

Munday, D. R., Johnson, H. L., & Marshall, D. P. (2013). Eddy saturation of equilibrated circumpolar currents. *Journal of Physical Oceanography*, *43*(3), 507–532. https://doi.org/10.1175/JPO-D-12-095.1

Murakami, S. (2011). Atmospheric local energetics and energy interactions between mean and eddy fields. Part I: Theory. *Journal of the Atmospheric Sciences*, *68*(4), 760–768. https://doi.org/10.1175/2010JAS3664.1

Olbers, D., Willebrand, J., & Eden, C. (2012). *Ocean Dynamics*. Berlin, Heidelberg: Springer Berlin Heidelberg. https://doi.org/10.1007/978-3-642-23450-7

Pacanowski, R. C., & Griffies, S. M. (2000). MOM 3.0 Manual. *Geophys. Fluid Dyn. Lab., Natl. Atmos. Admin., Princeton*, 682.

Plumb, R. A. (1986). Three-dimensional propagation of transient quasi-geostrophic eddies and its relationship with the eddy forcing of the time-mean flow. *Journal of the Atmospheric Sciences*. https://doi.org/10.1175/1520-0469(1986)043<1657:TDPOTQ>2.0.CO;2

Sasaki, H., Sasai, Y., Nonaka, M., Masumoto, Y., & Kawahara, S. (2006). An Eddy-Resolving Simulation of the Quasi-Global Ocean Driven by Satellite-Observed Wind Field Preliminary Outcomes from Physical and Biological Fields . *Journal of Earth Simulator*, *6*(October), 35–49. https://doi.org/10.32131/jes.6.35

Sasaki, H., Nonaka, M., Masumoto, Y., Sasai, Y., Uehara, H., & Sakuma, H. (2008). An Eddy-Resolving Hindcast Simulation of the Quasiglobal Ocean from 1950 to 2003 on the Earth Simulator. In *High Resolution Numerical Modelling of the Atmosphere and Ocean* (pp.

157–185). New York, NY: Springer New York. https://doi.org/10.1007/978-0-387-49791-4_10

Von Storch, J. S., Eden, C., Fast, I., Haak, H., Hernández-Deckers, D., Maier-Reimer, E., et al. (2012). An estimate of the Lorenz energy cycle for the World Ocean based on the 1/10°STORM/NCEP simulation. *Journal of Physical Oceanography*, *42*(12), 2185–2205. https://doi.org/10.1175/JPO-D-12-079.1

Thompson, A. F., & Garabato, A. C. N. (2014). Equilibration of the Antarctic Circumpolar Current by standing meanders. *Journal of Physical Oceanography*, *44*(7), 1811–1828. https://doi.org/10.1175/JPO-D-13-0163.1

Wu, Y., Wang, Z., & Liu, C. (2017). On the response of the Lorenz energy cycle for the Southern Ocean to intensified westerlies. *Journal of Geophysical Research: Oceans*, *122*(3), 2465–2493. https://doi.org/10.1002/2016JC012539

Youngs, M. K., Thompson, A. F., Lazar, A., & Richards, K. J. (2017). ACC meanders, energy transfer, and mixed barotropic-baroclinic instability. *Journal of Physical Oceanography*, *47*(6), 1291–1305. https://doi.org/10.1175/JPO-D-16-0160.1

Youngs, M. K., Flierl, G. R., & Ferrari, R. (2019). Role of residual overturning for the sensitivity of southern ocean isopycnal slopes to changes in wind forcing. *Journal of Physical Oceanography*, *49*(11), 2867–2881. https://doi.org/10.1175/JPO-D-19-0072.1

Zhai, X., & Marshall, D. P. (2013). Vertical eddy energy fluxes in the North Atlantic subtropical and subpolar gyres. *Journal of Physical Oceanography*, *43*(1), 95–103. https://doi.org/10.1175/JPO-D-12-021.1